 https://doi.org/10.3311/PPci.41175

Periodica Polytechnica Civil Engineering, 69(4), pp. 1092–1107, 2025

Investigation of Wind Loading on a Multi-span Anticlastic Tensile Membrane Surface: A CFD Approach

Richárd Joao Rosa[1*], Krisztián Hincz[1]

[1] Department of Structural Mechanics, Faculty of Civil Engineering, Budapest University of Technology and Economics, Műegyetem rkp. 3., H-1111 Budapest, Hungary
[*] Corresponding author, e-mail: rosar@edu.bme.hu

Received: 02 June 2025, Accepted: 13 August 2025, Published online: 05 September 2025

Abstract

The determination of the wind loads of tensile membrane structures is of crucial importance during their design, since the extremely light weight of the structures can easily lead to severe wind effects on the doubly curved surfaces. According to the current state of the art, almost exclusively wind tunnel test is applied, which is the most reliable method today. On the other hand, the time and cost-consumption of the physical measurements, as well as the questions around the Reynolds number dependency of the wind loads, are serious bottlenecks of such an experimental method. Computational Fluid Dynamics offers an excellent and flexible tool to overcome such problems, but the currently available computational powers prevent the application of robust and high-fidelity scale-resolving methods. The paper deals with the Computational Wind Engineering-based determination of the mean wind loads on a doubly curved tensile membrane structure, applying the Reynolds-averaged Navier-Stokes framework. The conventional *k-ω* Shear Stress Transport and the recently developed generalized *k-ω* turbulence models are applied in the simulations. The latter model provides a set of tunable model parameters, where the modification of the coefficients is much clearer and straightforward compared to other turbulence closure models. By tuning the relevant parameter during the simulations, the second model provided significantly better results. The numerical results are validated against experimental data from previous wind tunnel measurements. The internal forces of the membrane in the principal directions of the orthotropic membrane material are computed, and the maximal values of the experimental and numerical-based distributions are compared.

Keywords

tensile membrane structure, wind loading, Computational Fluid Dynamics, Computational Wind Engineering, *k-ω* SST, GEKO

1 Introduction

Tensile membrane surfaces offer flexibility and numerous structural advantages for covering large span areas with minimal internal supports. On the other hand, the light weight of the structural form makes the surfaces highly vulnerable to environmental effects. Determining the wind loads is a crucial part of the design, since the effect usually governs the sizing of the membrane material and the wind cables. Due to the complex fluid mechanical phenomena encapsulated in the underlying physics of turbulent flows, determining these loads is significantly more complicated than the structural investigation itself. According to the current state of the art, mainly wind tunnel (WT) tests are applied, which is currently the most accepted and reliable method. On the other hand, physical modeling has some characteristics that must be mentioned. WT measurements are time- and cost-consuming, while the scaling of the results between the model and full-scales can be questionable in case of significant Reynolds number (Re) differences, which dependence is not explicitly known in some design cases. This is especially true for tensile membrane surfaces, where the smooth and doubly curved surface does not have well-defined separation zones.

The wind engineering analysis of tensile membrane surfaces has an extensive literature, with investigations mainly focusing on the WT-based wind load determination. On the other hand, Computational Fluid Dynamics (CFD) is a promising tool that can complement and partially replace physical measurements. Still, the currently existing questions around these methods' reliability, especially in the case of computationally affordable Reynolds-averaged Navier-Stokes (RANS) simulations, prevent their confident application today.

Cite this article as: Rosa, R. J., Hincz, K. "Investigation of Wind Loading on a Multi-span Anticlastic Tensile Membrane Surface: A CFD Approach", Periodica Polytechnica Civil Engineering, 69(4), pp. 1092–1107, 2025. https://doi.org/10.3311/PPci.41175

Rizzo et al. [1] and Rizzo [2] investigated membrane roofs with different footprints and geometric ratios, concluding that the shape of the footprint or the geometric parameters like the span-to-height ratio fundamentally change the wind load characteristics. Rizzo et al. [3] and Rizzo and Ricciardelli [4] provided standardized pressure coefficient maps for various tensile membrane shapes. Kandel et al. [5] investigated arch-supported tensile membranes considering different span-to-height ratios with closed and open structural configurations, finding that both the geometric features and the openness significantly affect the wind loads. Sun et al. [6] investigated an oval-shaped arch-supported tensile membrane surface. Pagnini et al. [7] investigated parabolic vaulted roofs under different wind conditions on an isolated structural model and also with the inclusion of the surroundings. Based on the results, the presence of the surroundings mainly causes quantitative differences in the peak values, and the qualitative global distribution can be described in the isolated model with reasonable accuracy. Based on the previous results, it is evident that the standardization of the results into codal form is impossible due to the sensitivity to the many design parameters, and the wind load analysis in the case of every real design problem needs to be carried out for the particular geometry. De et al. [8] numerically investigated a conic structure using the Large Eddy Simulation (LES) framework. It is noted that LES simulations have significantly higher confidentiality compared to RANS methods; on the other hand, the currently available computational resources do not allow their practical application for design purposes. One possible solution for this shortcoming is the application of GPU-based simulation, which harnesses the power of the high parallelization of the numerical problem. This has already been implemented by Papp et al. [9] for instance. Pool-Blanco et al. [10] and Pool-Blanco and Hincz [11] investigated an air-inflated membrane surface numerically and experimentally with and without end walls using RANS. Conic membrane surfaces were also investigated by Pool Blanco and Hincz [12]. Measurements on a full-scale structural configuration were carried out by Hoxey and Richardson [13] for plastic-clad greenhouses.

The Re dependency of the wind loads is probably the biggest bottleneck of WT-based investigations, where the limitation of the wind speed and blockage ratio significantly determines the applicable Re range. This dependency is always a crucial question in the case of curved shapes without pronounced sharp edges. Gromke et al. [14] investigated the Re dependency of membrane-covered hemisphere biogas tanks. Qiu et al. [15] investigated hemicylindrical roofs under different Re and surface roughness conditions. Colliers et al. [16] studied the effect on hyperbolic paraboloid structures experimentally and numerically using RANS simulations.

The current paper deals with the Computational Wind Engineering (CWE) investigation of a multi-span tensile membrane surface close to a hemicylindrical shape, focusing on the mean pressure coefficient distribution using the RANS framework. Two different turbulence models were applied, the conventional k-ω Shear Stress Transport (SST) and the recently developed generalized k-ω (GEKO) models. The latter allows a much more straightforward tuning of the model *via* free parameters, with each parameter having a well-defined effect. Hence, after the initial identification of the problems of the turbulence model, the parameters can be modified to improve results. The numerical results for a particular geometry were validated based on the experimental results of the same structure carried out by Hincz et al. [17].

2 Numerical model

2.1 Geometry

The dimensions of the full-scale structure are shown in Fig. 1. The investigated scale of the prototype model 1:250, while the ratio of the velocities is 11.6 m/s: 30 m/s (~ 1:2.5) due to the limitations of the applied WT. Hence the combined ratio of the Re is around 1:700.

The numerical flow domain is depicted in Fig. 2. The correct determination of the domain sizes (inlet-outlet and symmetry plane distances from the structure) requires detailed analysis to ensure that the applied dimensions do not influence the flow field around the area of interest, i.e., the membrane surface. The $5 \times H$ and $15 \times H$ dimensions (where H is the characteristic length scale, the height of the structure) between the structure and the inlet/side planes, as well as between the structure and the outlet plane, can be applied as a starting point for the analysis. The current study extended these distances to $10 \times H$ and $20 \times H$, respectively, with no experienced effects on the monitored results (pressure forces on the surface). The blockage ratio of the model with the dimensions of the flow domain depicted in Fig. 2 is around 3%.

The applied semi-structured mesh is illustrated in Fig. 3. At the outer parts of the domain, a structured mesh with hexahedral elements was used to align the elements with the principal flow direction to reduce the effect of numerical diffusion in the simulations. In contrast, the innermost

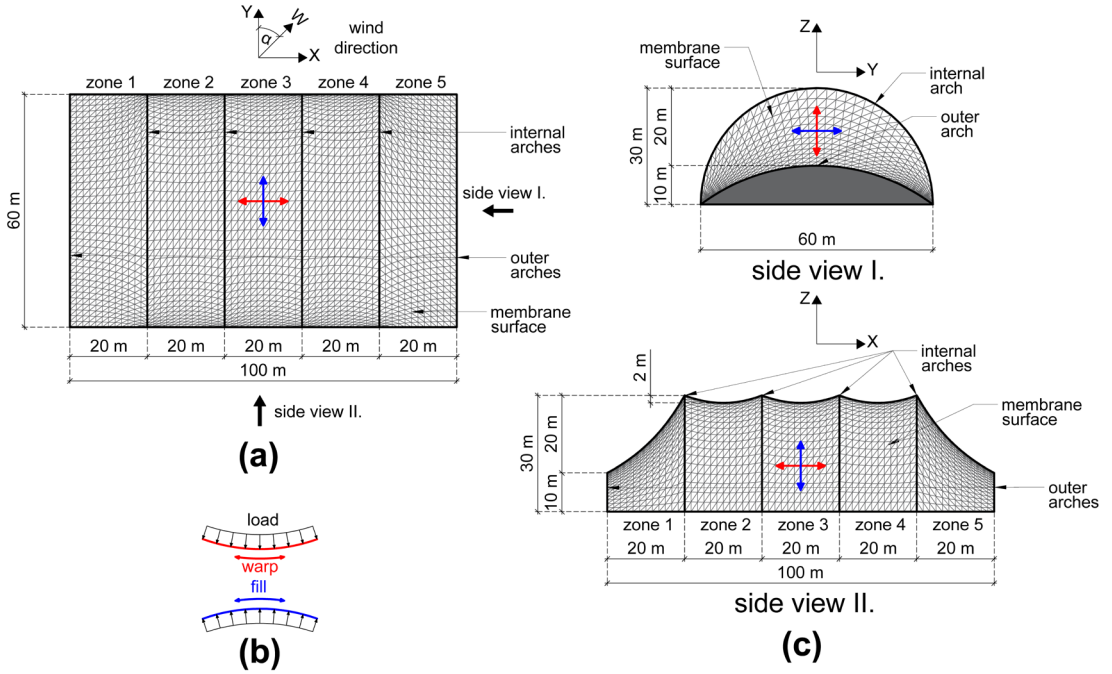

Fig. 1 Structural configuration and dimensions of the investigated tensile membrane: (a) top view; (b) warp and fill fiber directions; (c) side views

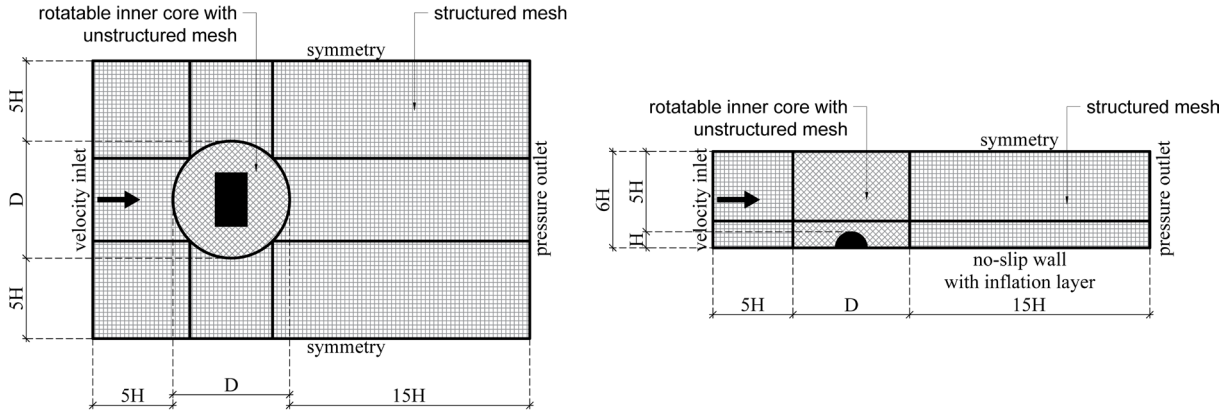

Fig. 2 Dimensions of the flow domain, boundary definition, and mesh structure

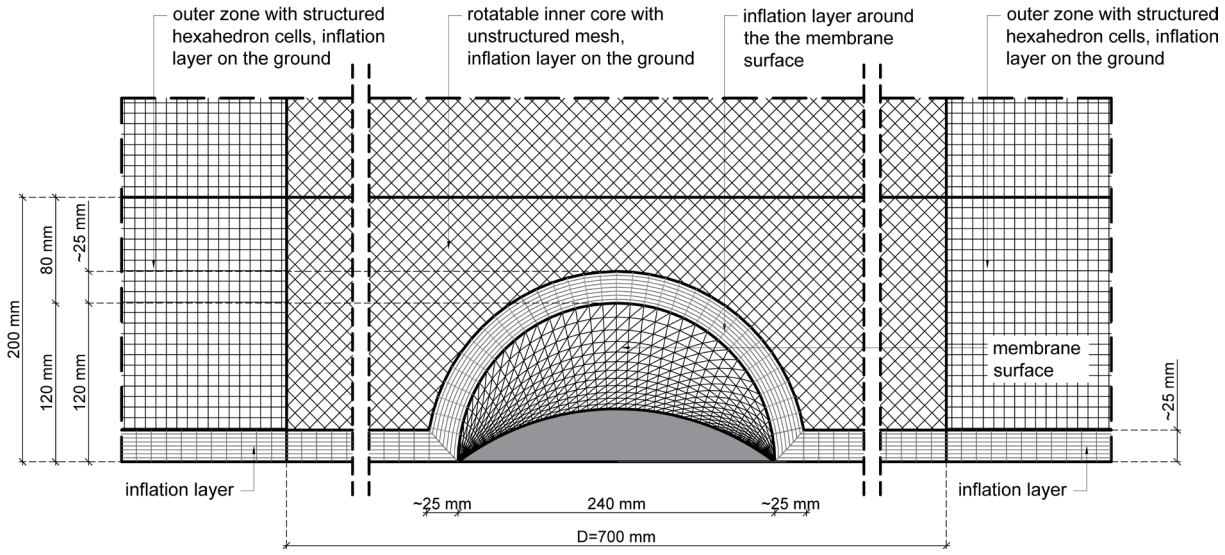

Fig. 3 Structure of the mesh around the membrane surface

part of the flow with the complex shape of the anticlastic membrane structure was discretized using tetra and prism elements to ensure sufficiently large element quality.

Due to the nature of the approximations used in Finite Volume Method (FVM) based CFD simulations, the results can be significantly improved with refined mesh density. The current investigation applied three different meshes to carry out a mesh independence study. Based on initial simulations, the cell size in the outer (structured) part of the mesh did not impose considerable effects on the monitored results (surface pressure forces of the membrane) below 25 mm average cell size (the investigated sizes were 25, 15 and 10 mm). Hence in the later studies the 25 mm edges length was applied which was necessary due to the intense boundary layer refinement on the bottom ground. This can result in large aspect ratios without proper discretization in the wall-normal direction and poor element quality. On the other hand, the intense refinement of the innermost part is of fundamental importance. The effect of the mesh face density along the membrane surface and the element sizes around the structure were both analyzed. The details of the meshes are illustrated in Table 1.

2.2 Boundary conditions

The inlet velocity profiles of the numerical and experimental analyses corresponded to the Atmospheric Boundary Layer (ABL) wind speed profile of the EN 1991-1-4:2005 standard [18] for Terrain Category II. The logarithmic velocity profile requires an intense boundary layer mesh refinement (inflation layer) on the bottom ground of the domain to ensure correct y^+ values (<5) for the low Re formulation of the applied turbulence models. The velocity profiles are shown in Fig. 4. The profiles of the wind velocity $v(z)$, the turbulence kinetic energy $k(z)$, and the specific dissipation rate $\omega(z)$ are given by:

$$v(z) = \frac{u^*}{K} \ln\left(\frac{z + z_0}{z_0}\right), \tag{1}$$

$$k(z) = \frac{u^{*2}}{\sqrt{C_\mu}}, \tag{2}$$

$$\omega(z) = \frac{u^*}{K\sqrt{C_\mu}} \times \frac{1}{z + z_0}, \tag{3}$$

where $K = 0.41$ is the von Kármán constant, z_{ref} is the reference or characteristic height of the model, u_{ref} is the reference velocity at z_{ref}, $z_0 = 0.05$ m is the roughness length corresponding to Terrain Category II [18], $C_\mu = 0.09$ is empirical constant, and u^* is the friction velocity computed as:

$$u^* = \frac{u_{ref} \times K}{\ln\left(\frac{z_{ref} + z_0}{z_0}\right)}. \tag{4}$$

2.3 Physical model

The numerical simulations are based on the RANS framework. It is noted that flows around complex surfaces are primarily investigated by time-dependent and scale-resolving models (LES or RANS-LES hybrids) in the literature, since the Reynolds-averaging with the applied turbulence models usually cannot describe the transient phenomena (e.g., vortex shedding of conical surfaces) occurring in the flow. On the other hand, these models currently require significant computational time. Hence, applying RANS simulations, at least for preliminary design with acceptable accuracy, would be desirable. Two different turbulence models were investigated in the current paper to gain insight into the applicability of the RANS approach.

WT measurements previously determined and thoroughly investigated the flow field [17]. It is noted that the investigated shape has fundamentally different characteristic flow patterns under different wind directions. Namely, the simultaneous presence of the smooth, doubly curved surface and the sharp edges between the adjacent zones exhibits two different wind load characteristics. On the one hand, the sharp edges determine the separation zones of the fluid; separation is well-defined in wind directions where these edges meet close to perpendicular with the incoming wind. In these cases, the Re dependence of the pressure forces is also expected to be negligible. Another fundamentally different flow field is expected

Table 1 Mesh parameters

Properties		Unit	M1	M2	M3
Membrane surface	Number of faces/zone	[-]	864	3456	7776
	Zonal subdivision (arch/long)		36/12	72/24	108/36
Inner mesh	Average edge length	[mm]	10	10	5
Inflation layer	Maximum value of y^+	[mm]	~ 2.5	~ 2.5	~ 1
	Total thickness	[mm]	25	25	25
Number of elements		[-]	~ 3 000 000	~ 4 500 000	~ 9 000 000

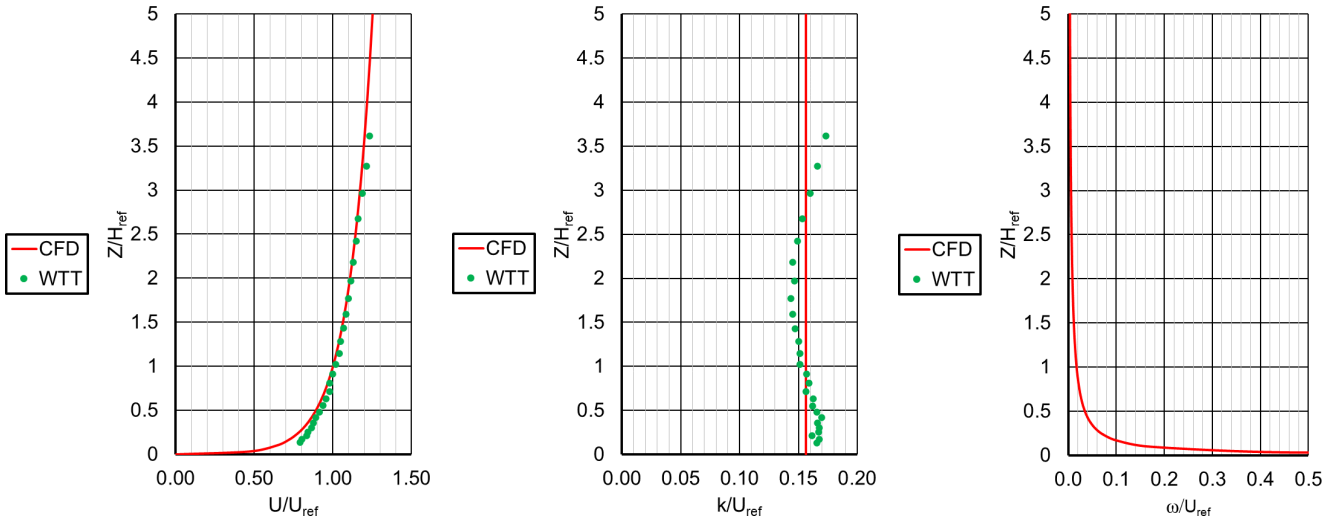

Fig. 4 Profiles according to EN 1991-1-4:2005 standard [18] Terrain Category II: (a) velocity; (b) turbulence intensity; (c) specific dissipation rate

at a perpendicular wind to the axis of the structure, where the smooth membrane surface controls the flow. Here, the flow separation can take different places under different Re. Finally, under skew wind, the mixed effect of the smooth curved surface and the sharp edges can interact with variable emphasis on the individual mechanisms. The strongest separations are expected under skew wind directions biased toward the plane of the arches, where the small angles between the flow and sharp edges might induce helically separating vortex formation. The identification of these three fundamental flow patterns was also made by Kandel et al. [5] for a similar configuration.

2.3.1 *k-ω* SST

Due to the different characteristic behaviors under various wind directions, applying different turbulence models might be necessary. It is traditionally known that the conventional *k-ω* SST turbulence model [19] combines the strengths of the standard *k-ε* and *k-ω* models by applying them in the regions of their favorable behavior and blending the models in the intermediate zones. On the other hand, it has already been shown that the *k-ε* model family outperforms this model in case of sharp-edges control the flow [20]. In the current paper, only the *k-ω* SST model was applied from the traditional turbulence closure formulations, since the emphasis is on using a novel approach provided by GEKO. For brevity, the equation system of the numerical simulation is introduced *via* the *k-ω* SST model in a simplified form (Eqs. (5) to (8)):

$$\frac{\partial u_i}{\partial x_i} = 0, \tag{5}$$

$$\frac{\partial u_i}{\partial t} + \frac{\partial u_i}{\partial x_j} u_j = g_i - \frac{1}{\rho}\frac{\partial p}{\partial x_j} + \left(\nu + \nu_T\right)\frac{\partial^2 u_i}{\partial x_j^2}, \tag{6}$$

$$\frac{\partial k}{\partial t} + \frac{\partial k}{\partial x_j} u_j = P_k - D_k + \frac{\partial}{\partial x_j}\left[\left(\nu + \sigma_k \nu_T\right)\frac{\partial k}{\partial x_j}\right], \tag{7}$$

$$\frac{\partial \omega}{\partial t} + \frac{\partial \omega}{\partial x_j} u_j = P_\omega - D_\omega + \frac{\partial}{\partial x_j}\left[\left(\nu + \sigma_\omega \nu_T\right)\frac{\partial \omega}{\partial x_j}\right] + \text{"blending term"}, \tag{8}$$

where u_i are the mean velocity components, p is the mean static pressure, ν and $\nu_T = \nu_T(\partial u_i/\partial x_i)$ is the kinematic and eddy viscosity respectively, the latter one containing the effect of the turbulence modeling with the expression of ν_T with the mean flow variables, g_i are the components of the body force. Equations (7) and (8) express the transport of the turbulent kinetic energy k and the specific dissipation rate ω, where P_k, P_ω and D_k, D_ω denote the production and dissipation of the quantities respectively, while the third terms express their diffusive transport with the σ_k and σ_ω turbulent Prandtl numbers. The unspecified last term in Eq. (8) is responsible for blending the standard versions of the *k-ω* and *k-ε* turbulence models. In the case of classical steady-state RANS, the first terms in the equations expressing the local change in the variables are zero; the only remaining term is the convective transport on the left-hand sides. The body force components g_i acting on the air parcels in Eq. (6) are also neglected for wind engineering purposes.

It is noted that the calibration of the conventional *k-ω* SST turbulence model is possible. e.g., for the modelling of wind turbines under light stall condition, where

the flow separation and reattachment are simultaneously present, the default model settings can lead to poor results (it is mentioned that the investigated flow around the tensile membrane surface in the skew wind directions and under wind perpendicular to the plane of the arches also characterized by the separation and reattachment, hence similar problems are expected there). To overcome such issues of the closure model, Younoussi and Ettaouil [21] calibrated the a_1 (directly influences the eddy viscosity) and β^* (parameter inside the turbulent kinetic energy production and dissipation terms) parameters inside the k-ω SST turbulence model, with different effects under different flow conditions. When separation and reattachment can be observed (light stall), significant improvement can be achieved. When no separation was observed, the calibration was ambient. Finally, under deep stall condition (no reattachment after separation), the calibrated model for the light stall condition led to worse prediction than the default model. On the other hand, it is also reported that the modified parameter settings of the recalibrated model can significantly detune the original calibration based on the simple flow cases (e.g., flat plate boundary layer). Moreover, the effect of the individual parameters is not as well-defined and separated as in the case of GEKO. Hence, the optimal parameter setting determination leads to a much more circumstantial process, which is not covered in the current paper.

2.3.2 GEKO

The recently developed GEKO turbulence model [22] enables the application of a single turbulence model for many flow cases. A significantly more straightforward tailoring of the model with tunable model parameters is possible compared to the traditional closure models, where the effect of each parameter is not as well-defined and separated as in GEKO, and minor changes can sometimes lead to drastically altered flow fields. Also, different turbulence models might be necessary to investigate the same structural system under different wind directions. Moreover, GEKO can also capture secondary flow patterns under RANS modeling, where the conventional turbulence models fundamentally fail. For instance, Lukács and Vad [23] investigated square-to-square sudden expansions, while Lyu et al. [20] investigated wedge-shaped 2D obstacles. The main parameters of GEKO are briefly introduced in Table 2. From the six main parameters, the two relevant coefficients of the current investigation and their role are the followings:

- C_{sep} (separation parameter) is the most fundamental, enabling flow control in bluff body aerodynamics, where the separations can be sensitive to the model settings. This is primarily the case in flows driven by adverse pressure gradients, where the wall shear stress is combined with the further decelerating effect of the pressure field. C_{sep} exerts its influence through the modification of the Eddy Viscosity Ratio (EVR): by increasing its value, the EVR decreases, leading to earlier flow separation.
- The spreading rate of the separated flow and the shear layer can be controlled with C_{mix} (mixing parameter). Increasing its value increases the shear layer's spreading rate and the separation bubble's turbulence level. It is noted that the boundary layer is protected by a blending function that deactivates C_{mix} in that region. The size of the protected zone can be influenced by another sub-parameter (C_{turb}).

3 Results

For the validation of the numerically determined wind loads, the CFD results are compared to the experimental results [17] based on the non-dimensional pressure coefficient parameter:

$$\overline{c}_p = \frac{\overline{p}(t) - p_0}{\overline{q}_h} = \frac{\overline{p}(t) - p_0}{0.5\rho\overline{u}_h^2}, \tag{9}$$

where $\overline{p}(t)$ is the mean value computed from the time series of the static pressure at the given point, p_0 is the reference/atmospheric static pressure, $\overline{q}_h$ is the dynamic pressure at the model's height, ρ is the air density, and $\overline{u}_h$ is the streamwise mean velocity measured at the model's height.

Table 2 Parameters of the GEKO turbulence model

Coefficient	Effect	Range of values	Default value
C_{sep}	Controls the separation points or lines.	0.7–2.5	1.75
C_{nw}	It affects the inner part of boundary layers. Leads to higher wall shear by increasing	−2.0–2.0	0.5
C_{mix}	Determines the spreading rate of free shear flows	0–1.0	Calculated from C_{sep}
C_{jet}	Affects mostly jet flows	0–1.0	0.9
C_{corner}	For the modeling of secondary flows in pipe flows	0–1.5	1.0
C_{curv}	Curvature correction	0–1.5	1.0

180 pressure detection points were distributed throughout the surface, 36 measurement points located in each panel. The layout of the measurement nodes is presented in Fig. 5.

Besides the pressure coefficient distributions, the non-dimensional wind force coefficients in the main coordinate directions were also calculated and compared:

$$\bar{c}_i = \frac{\bar{F}_i}{\bar{q}_h A_i} = \frac{\sum \bar{c}_{pj} A_j \boldsymbol{n}_j^T \boldsymbol{e}_i}{A_i}, \tag{10}$$

where $i = \{x, y, z\}$ represents the x, y and z directions, $\bar{F}_i$ is the component of the mean resultant wind force, A_i is the projected area of the zonal surface perpendicular to the investigated coordinate direction and $\bar{q}_h$ is the dynamic pressure at the reference height. For the calculation of $\bar{F}_i$, $\bar{c}_{pj}$ is the mean pressure coefficient, A_j is the surface area, and $\boldsymbol{n}_j$ is the unit normal vector of the j^{th} surface element, while $\boldsymbol{e}_i$ is the unit vector in the i^{th} coordinate direction. The summation in Eq. (10) refers to every surface element of a zone or the whole structure, depending on the comparison.

3.1 Mesh independence study

The results of the mesh independence study (see Table 1) are presented in Table 3. Table 3 contains the global wind force coefficients computed based on Eq. (10).

Based on the results, the following observations can be made:

- k-ω SST: at 0° and 90° wind directions, the study suggests mesh insensitivity. In contrast, no convergence was achieved amongst the applied meshes under skew wind. Hence, the model can be used in the "pure" flows, while in the skew wind directions, it is inadequate to capture the complex transient flow.
- GEKO: the model still provided slight mesh dependency in the skew wind direction, although the differences between the results with the M2 and M3

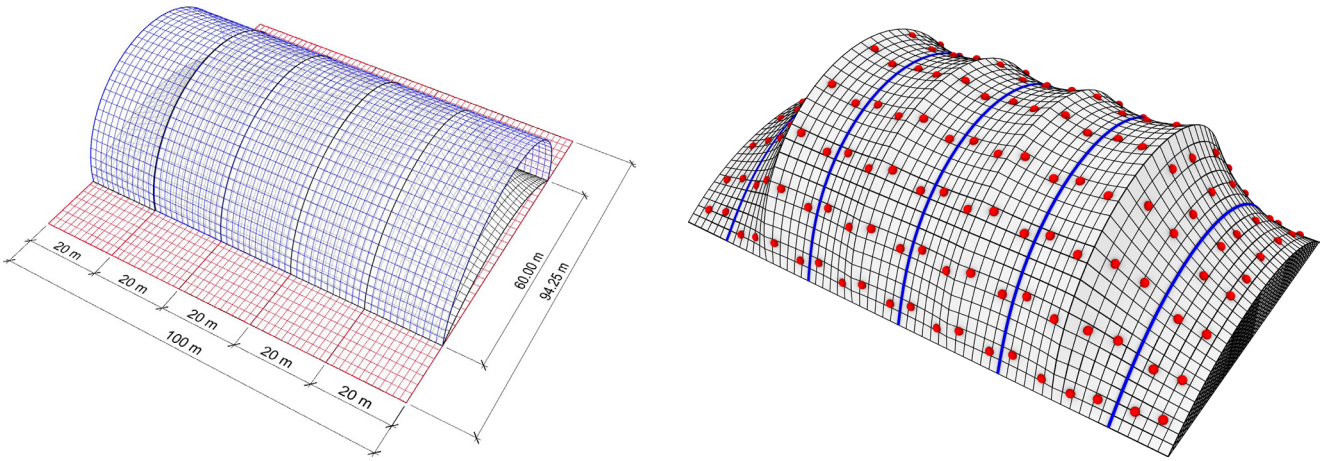

(a) (b)

Fig. 5 Unfolded structure for the easier presentation and interpretation of the results and location of the measurement points in the WT model: (a) topologically identical half-cylindrical mesh (blue) and the unfolded mesh (red) for the presentation of the pressure coefficient distribution; (b) the pressure detection points (red) and the midlines of the zones (blue) for the turbulence model comparison

Table 3 Global wind force coefficients for three selected wind directions and meshes (the corresponding values of the individual meshes are highlighted with the same color (M1: beige color; M2: green color; M3: blue color))

Force component	Mesh	0°			45°			90°		
		k-ω SST	GEKO		k-ω SST	GEKO		k-ω SST	GEKO	
			C_{sep} = 1.00	C_{sep} = 1.75		C_{sep} = 1.00	C_{sep} = 1.75		C_{sep} = 1.00	C_{sep} = 1.75
F_x	M1	0.01	0.01	0.01	0.38	0.56	0.47	0.49	0.67	0.62
	M2	0.00	0.00	0.00	0.38	0.51	0.35	0.48	0.63	0.58
	M3	0.00	0.00	0.00	0.29	0.46	0.32	0.48	0.66	0.56
F_y	M1	0.35	0.39	0.40	0.46	0.43	0.52	0.00	0.00	0.00
	M2	0.36	0.40	0.41	0.45	0.46	0.58	0.00	0.00	0.00
	M3	0.36	0.40	0.40	0.54	0.49	0.60	0.00	0.00	0.00
F_z	M1	1.97	2.35	2.15	2.06	2.09	2.02	1.16	1.14	1.12
	M2	1.91	2.29	2.07	1.97	2.06	1.85	1.15	1.14	1.12
	M3	1.91	2.27	2.05	1.71	1.99	1.78	1.19	1.15	1.12

meshes decreased considerably compared to *k-ω* SST. From the two presented separation parameters in Table 3, the smaller value (C_{sep} = 1.00) provided better results (by increasing the EVR). Comparing *k-ω* SST and GEKO with C_{sep} = 1.00, the largest differences in the *x*/*y*/*z*-directional wind force coefficient in the 45° wind direction decreased from 25% (0.38–0.29) to 3% (0.51–0.46), from 20% (0.45–0.54) to 3% (0.46–0.49) and from 13% (1.97–1.71) to 4% (1.85–1.78), respectively.

In summary, GEKO provided significantly improved results compared to *k-ω* SST. In the following simulations of the paper, the M2 mesh will be applied considering both the accuracy and the mesh size.

3.2 Turbulence model assessment

The initial simulations were carried out using the *k-ω* SST turbulence model and the default setting of GEKO. The mesh independence study introduced in Section 3.1 already showed that *k-ω* SST cannot handle the transient phenomena of the flow under skew wind directions.

Based on the initial experiences, the model parameters of GEKO (C_{sep} and C_{mix}) were changed to tailor the turbulence model to mimic the WT-based mean pressure coefficient distribution best. It is noted that the effect of C_{mix} in the investigated wind directions were negligible on the $\overline{c}_p$ distributions, mainly since the parameter is shielded in the boundary layer with a blending function. Hence, only the effect of the C_{sep} parameter will be introduced in Section 3.3 thoroughly. The Mean Average Error (MAE) values computed from the different C_{sep} values are illustrated in Fig. 6, where the other coefficients were kept at their default values (see Table 2).

Based on Fig. 6, the most significant effect of C_{sep} is observable under small wind directions (0°–20°). Hence,

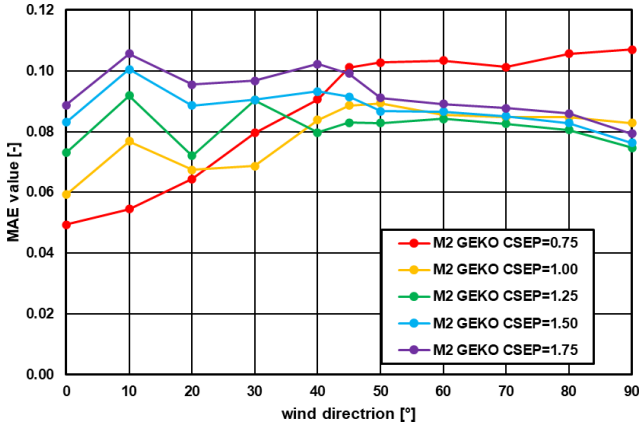

Fig. 6 MAE values computed from CFD results with different C_{sep} values

0° wind direction is selected to illustrate the separation control over the surface with C_{sep}. The mean pressure coefficient $\overline{c}_p$ distributions are compared under five different C_{sep} values (0.75–1.75) in Fig. 7 along the midlines of the zones (Figs. 1 and 5). Fig. 7 also depict the results computed with *k-ω* SST, the WT results of the smooth surface, and the roughened surface applying trip wires based on Hincz et al. [17]. In the experimental setup, the trip wires with 1 mm diameter were glued to the surface driven perpendicularly to the supporting arches. The full-scale measurements of Hoxey and Richardson [13] are also Fig. 7.

The following conclusions can be made:

- It is noted that even the turbulence model switch from *k-ω* SST to the default GEKO enhanced the results, especially in the skew directions, where *k-ω* SST fails considerably, with mesh convergence issues. This can be originated from the property of GEKO that it can handle transient flow features (e.g., secondary flows in duct tapes).
- Based on Fig. 6, the reduction of C_{sep} had the largest impact under small wind directions (wind close to parallel to the plane of the arches). At 0° wind, the reduction of the parameter continuously improved the results, and gave the best accuracy between 0°–20°. After that initial phase, the 0.75 value quickly turned out to be the worst setting, indicating that the significantly increased EVR gave poor results in the pronounced effect of the edges. Based on Fig. 7, the results also fit nicely to the large-scale measurements of Hoxey and Richardson [13] in the middle zones.
- The reason for the positive effect of the decreasing value of C_{sep} is that by increasing the EVR, the turbulent flow can pump more energy into the boundary layer, which in turn can attach further to the surface. Consequently, the flow separation can be delayed, which can be seen in the increased and shifted peak negative $\overline{c}_p$ value toward the rear part of the surface.
- The 1.0–1.75 regime provided minor differences in the MAE values over 50° wind direction. It is noted that the further increase of the parameter to 2.50 also resulted in a negligible difference in the results in the corresponding wind directions.
- C_{sep} = 1.0 seems to be an "optimal" setup considering every analyzed wind direction.

3.3 Force coefficient comparison

Based on the mesh independence study and the parameter evaluation of GEKO, the M2 mesh with C_{sep} = 1.00 is considered in the results shown in Sections 3.3 to 3.5.

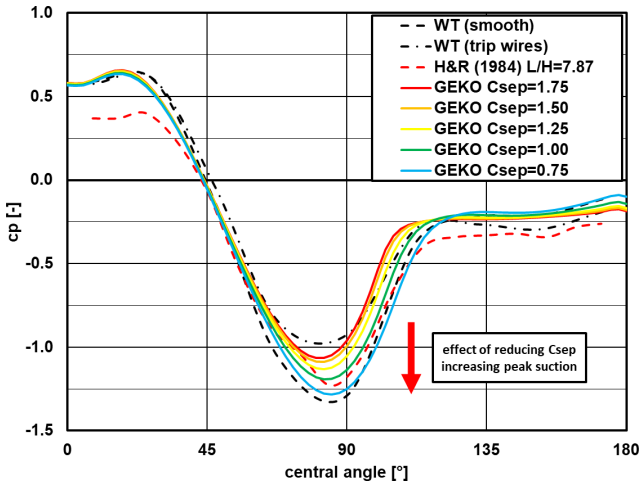

(a)

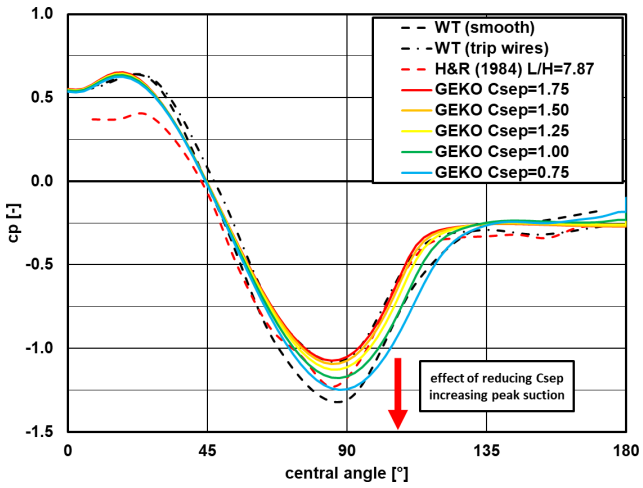

(b)

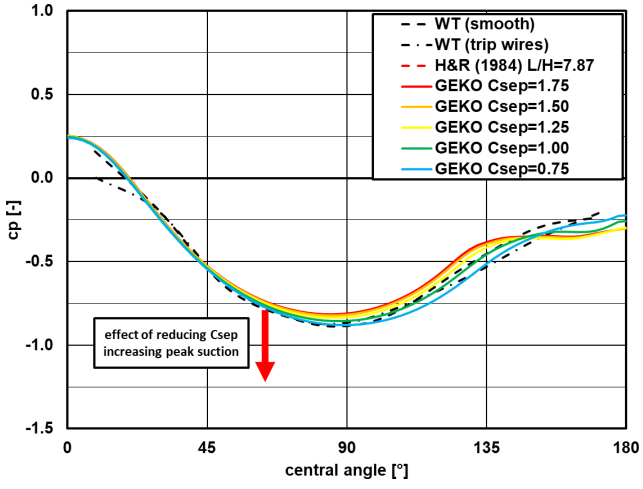

(c)

Fig. 7 Pressure coefficient distribution under 0° wind direction (wind parallel to the plane of the arches) determined by WT measurements, CFD simulations and large-scale on-site measurements [13] along the midlines of the individual zones: (a) Zone 3; (b) Zone 2 and 4; (c) Zone 1 and 5

The numerically and experimentally determined force coefficients under the investigated eleven wind directions are presented in Fig. 8 for the three main coordinate directions (c_x, c_y and c_z).

With the zonal comparison of the force coefficients, the varying accuracy of the CFD approximation can be observed. In general, the numerically calculated force coefficients captured the WT distribution correctly, with the exception of Zone 5 over 20° wind direction in the y-coordinate direction, where the numerical results

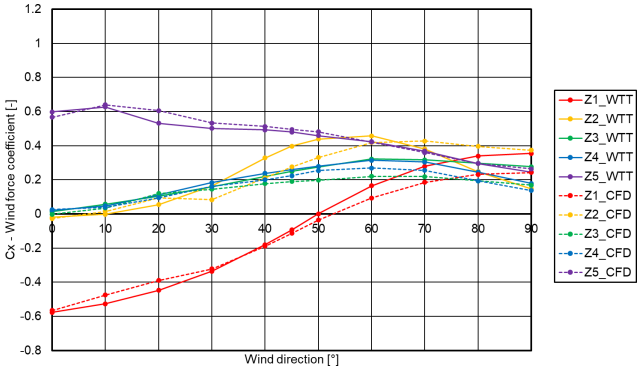

(a)

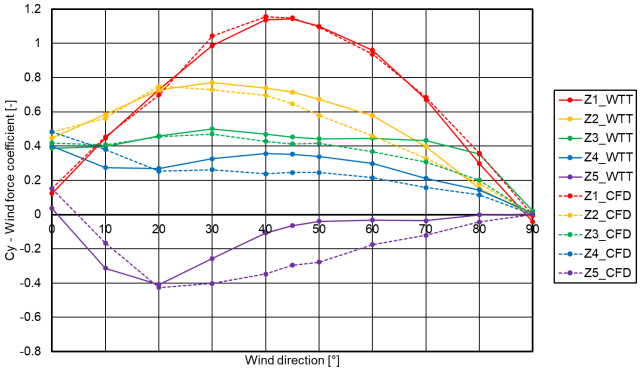

(b)

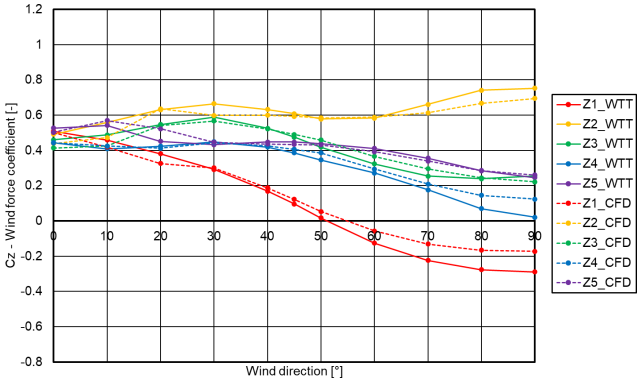

(c)

Fig. 8 Force coefficient comparison of the five roof zones based on WT measurements and CFD (GEKO, C_{sep} = 1.00) simulations: (a) c_x; (b) c_y; (c) c_z force coefficient under the investigated wind directions

are significantly larger than the experimental values. Two comments need to be added here to the evaluation of the results and for a possible explanation of this difference:

- The approximation of the pressure distribution with the numerical model is generally good, with the exception of the mentioned zone. Here the error is localized.
- At Zone 5, the CFD model provided significantly larger pressure forces in the y-direction, while the x- and z-directional force coefficients are correctly captured. This indicates that the difference is localized around the vicinity of the sharp edge formed by the internal arch between Zone 4 and Zone 5. Here, large negative peak $\bar{c}_p$ values are detected in the numerical simulations, which are extremely quickly decreasing toward the interior of Zone 5. In the WT measurements, no pressure detection points were located in the close vicinity of this separation line. Hence, the WT-based distribution can only be determined *via* extrapolation there, and no direct information could be gathered from the corresponding zone.

3.4 Pressure coefficient distribution

The pressure coefficient distributions are presented in a half-cylindrical mesh topologically identical to the doubly curved membrane surface, according to Fig. 5. The mapping of the results to the planar-foldable surface made the presentation and interpretation of the distributions easier.

The mean pressure coefficient distributions for the eleven investigated wind directions determined by CFD simulations are illustrated in Figs. 9 and 10. The WT-based distribution for six selected wind directions is presented in Hincz et al. [17]. The fluctuating pressure coefficients are depicted in Figs. 11 and 12, while the difference between the CFD and WT-based results is illustrated in Figs. 13 and 14. The detailed analysis of the distributions can be found in Hincz et al. [17], here, only a few important remarks are given:

- Note the three fundamentally different pressure coefficient distribution patterns at 0°, 90°, and skew wind directions. A repeated pattern of the pressure distribution of the individual zones can be observed between 0°–60° wind in each zone, containing a stagnation zone with positive pressure forces, a separation zone with negative peak values, and approximately constant suction at the separation bubble. At 0° wind, the separation is located around the apex of the surface, while with the growing angle of the incoming flow, it is shifted to internal arches with large peak suction on their leeward side.
- Over 60° wind direction, the last zones are fully located in the separation bubble of the flow, indicated by the almost constant pressure distribution. Hence, the large, separation-induced suction vanishes behind the rear arches, only remaining behind the first internal arch.

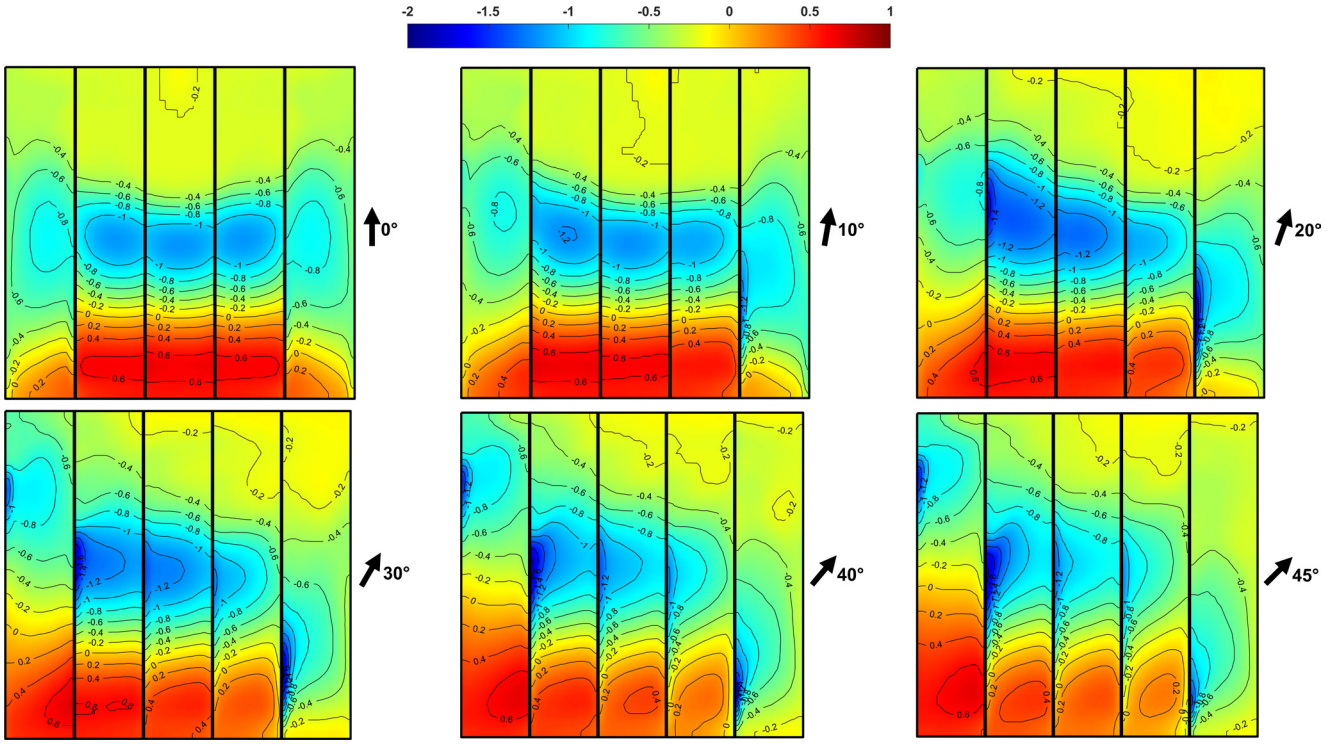

Fig. 9 Mean pressure coefficient $\bar{c}_p$ distribution under 0°–45° wind directions determined by CFD simulation (GEKO, C_{sep} = 1.00)

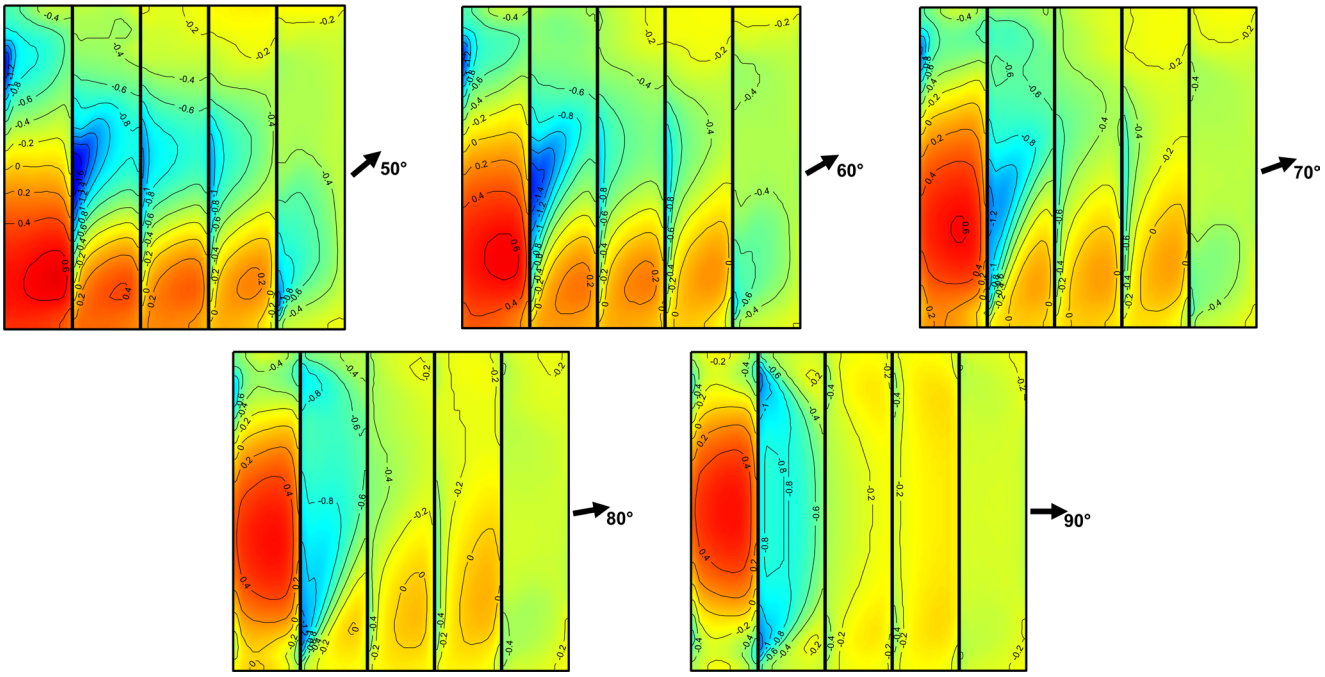

Fig. 10 Mean pressure coefficient $\bar{c}_p$ distribution under 50°–90° wind directions determined by CFD simulation (GEKO, C_{sep} = 1.00)

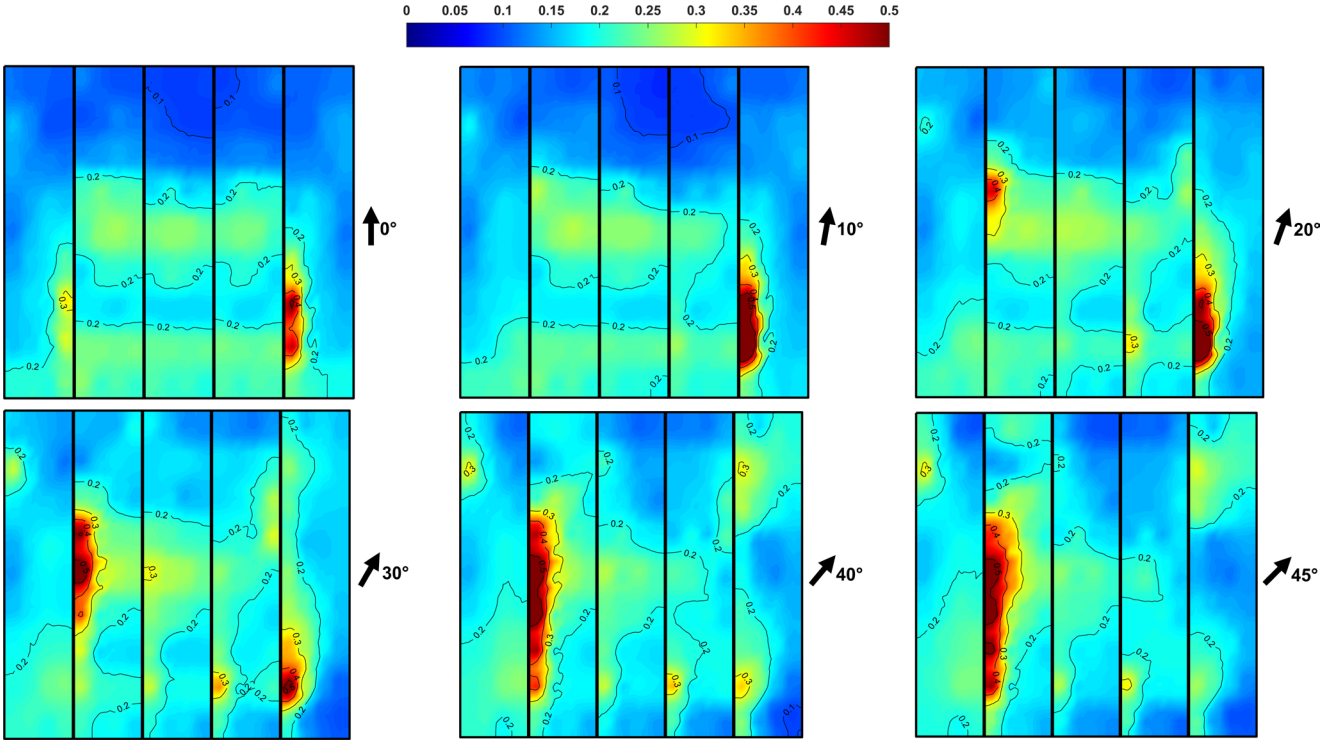

Fig. 11 Fluctuating pressure coefficient c'_p distribution under 0°–45° wind directions determined by WT measurements

- At skew wind directions, the internal arches determine the separation zone of the flow, where large suction forces are detected. These negative pressure forces are rapidly decreasing. This effect is most probably indicated by the helically separating vortices caused by the skew angle between the sharp edges and the incoming flow.
- The difference between the WT and CFD results is largest around the zones with the largest fluctuating components. The fluctuating c'_p maps and the difference of the experimental and numerical $\bar{c}_p$ maps nicely resemble each other.
- In some cases (10°–40°), the CFD simulations correctly determined the magnitude of the peak suction

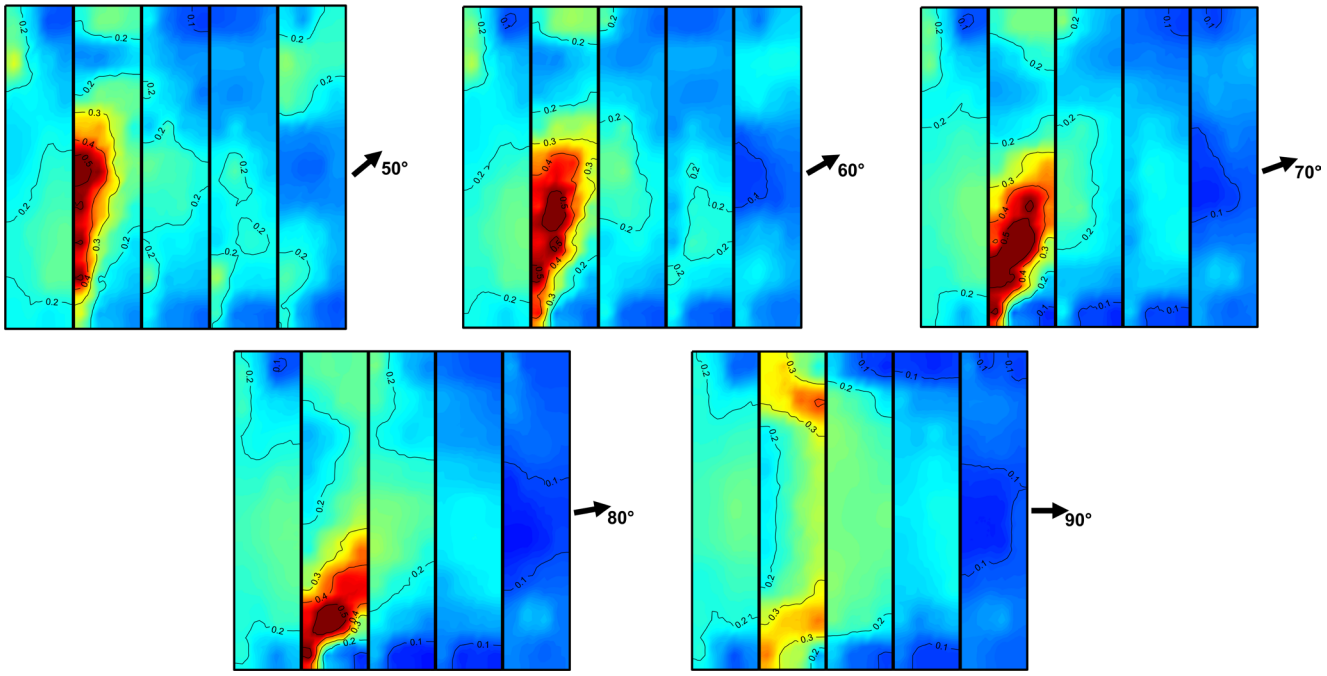

Fig. 12 Fluctuating pressure coefficient c'_p distribution under 50°–90° wind directions determined by WT measurements

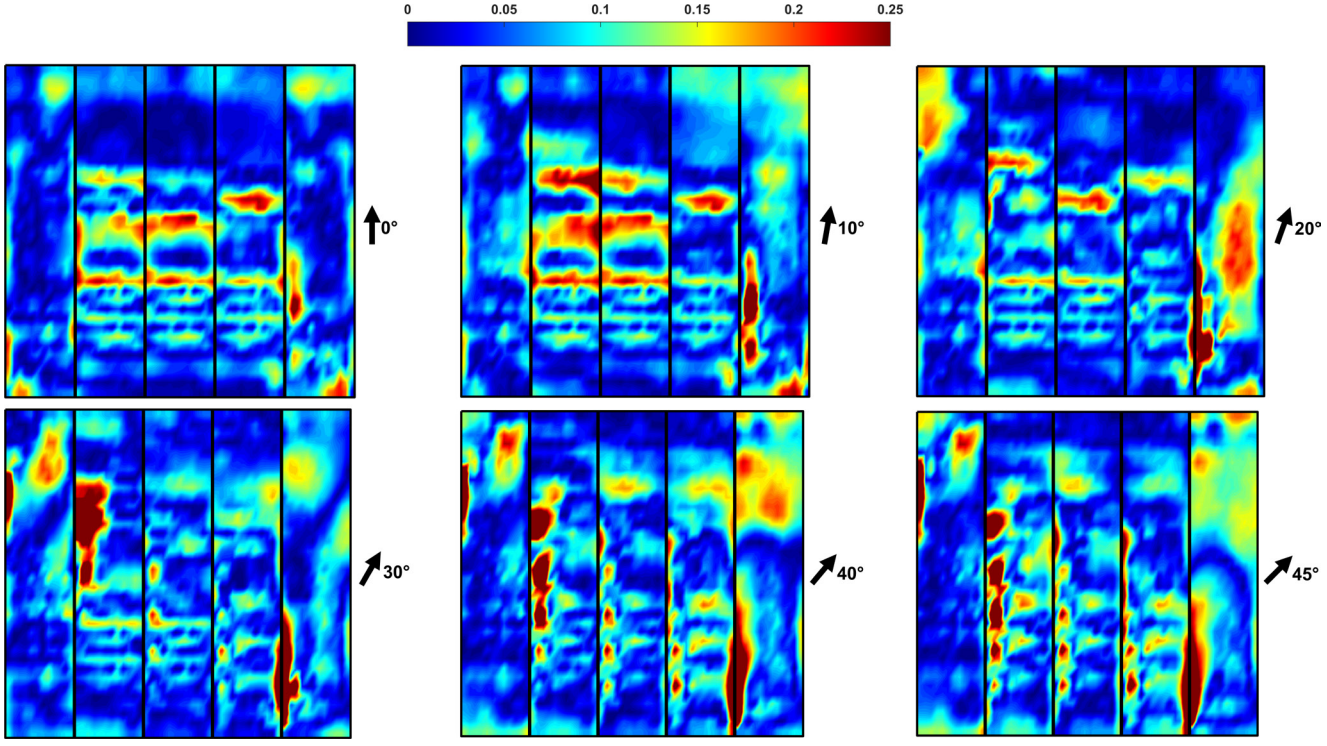

Fig. 13 Difference of the WT and CFD-based (GEKO, C_{sep} = 1.00) mean pressure coefficient $\bar{c}_p$ distributions under 0°–45° wind directions

forces. However, the extension of the large suction zone is considerably smaller in the CFD-based distribution. These are the locations of the previously mentioned helical vortex separation zones, where the more accurate determination of the phenomena would require a scale-resolving numerical approach (e.g., LES simulations). However, GEKO can still determine these peak suction forces behind every internal arch, while the application of *k-ω* SST led to poor results here. It is noted here that the largest differences of the WT and CFD-based internal membrane forces of the structure (introduced in Section 3.5) are caused by this property of the numerical results.

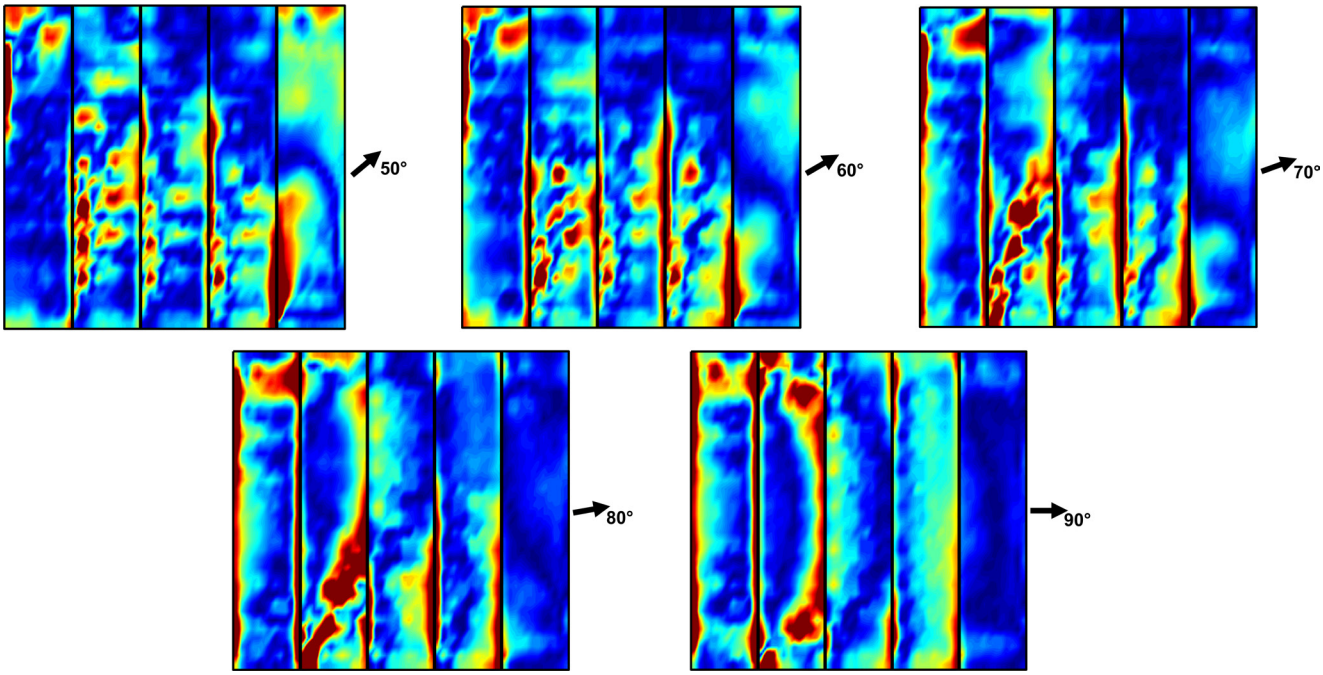

Fig. 14 Difference of the WT and CFD-based (GEKO, C_{sep} = 1.00) mean pressure coefficient $\bar{c}_p$ distributions under 50°–90° wind directions

3.5 Membrane forces

One of the most important outputs of the structural analysis of membrane structures is the membrane force distribution in the orthotropic material. The comparison of the membrane forces in the warp and fill fiber directions based on the experimental and CFD-based pressure distributions provides valuable information about the reliability of the CFD results from a structural point of view. The membrane forces were determined based on the method presented by Hincz [24]. The warp direction is perpendicular to the arches (Fig. 1), and the membrane material is fixed to the arches and the straight edges. The wind pressure increases the force in the fibers in warp direction; the wind suction increases the force in the fibers in fill direction. The applied average prestress in the construction shape was 22 kN/m, and the presented membrane forces correspond to 1 kN/m^2 dynamic wind pressure. The same modulus of elasticity (E = 1600 kN/m) was considered in the orthogonal warp and fill directions.

For the illustration of three characteristic membrane force distributions, Fig. 15 presents the internal forces under 0°, 45° and 90° wind directions in the principal directions of the membrane material. Fig. 16 presents the maximum membrane forces in warp and fill directions. In the warp direction, there is a very good agreement between the WT and CFD-based membrane forces; the most significant difference is less than 5%. The slight deviation is consistent with the good approximation of the pressure distribution on the windward side. In contrast, the maximum deviation in the weft direction is almost 14%, which is observed in Zone 2, at a wind direction of 30°. The reason is the relatively significant difference in extension of the peak negative pressure coefficient zone behind the supporting arch between Zone 1 and Zone 2 at wind directions between 30°–50° (Fig. 14).

4 Conclusions

The current paper investigated the applicability of RANS-based CFD simulations for the determination of the mean wind loading of an arch-supported tensile membrane structure. The doubly curved shape of the structure and the sharp edges formed by the internal supporting arches are simultaneously present and shape the flow pattern around the structure, creating complex flow phenomena. Based on the results of the applied k-ω SST and GEKO turbulence models, the following conclusion can be drawn:

- GEKO significantly outperformed the conventional k-ω SST model in every analyzed wind direction. The latter model also failed to provide mesh convergence under skew wind directions, due to the strong transient phenomena (helical vortex separation) in several flow directions.
- The C_{sep} parameter of GEKO can adequately control the adverse pressure gradient-driven flow separation (0°–20°). By reducing C_{sep} and increasing the EVR, the separation can be delayed enabling further

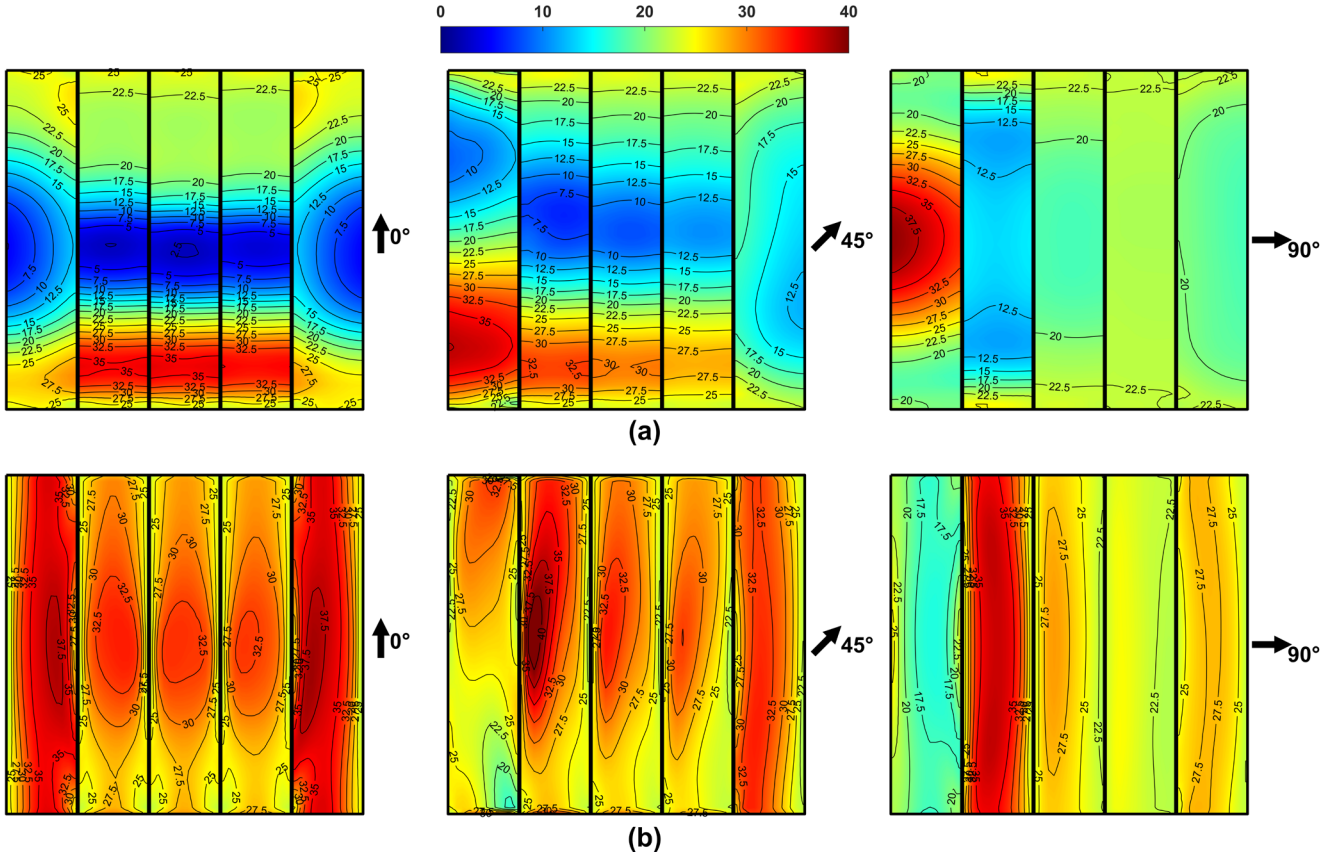

Fig. 15 Membrane force distribution determined by WT measurements: (a) warp direction; (b) fill direction

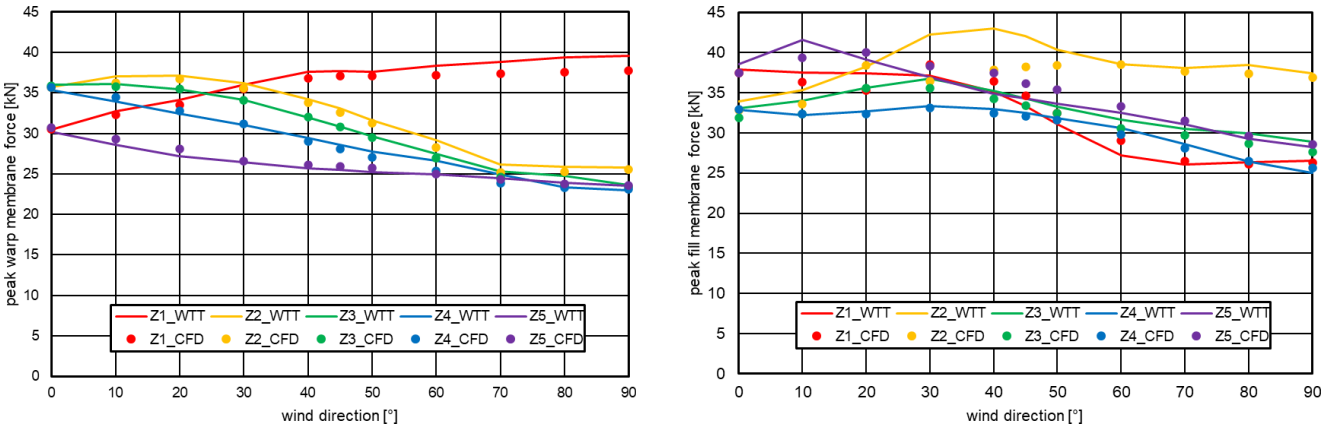

(a) (b)

Fig. 16 Membrane force maxima in the investigated wind directions determined by WT measurements and CFD simulations (C_{sep} = 1.00): (a) warp direction; (b) fill direction

acceleration of the flow along the surface, finally creating larger suctions. In the sharp edge-controlled flow regime (50°–90°), the $\overline{c}_p$ distribution is insensitive to the parameter setting. C_{mix} did not influence the results considerably.

- C_{sep} = 1.00 provided the best results globally.
- The wind force coefficients characterizing the zonal effect of the wind loads provided good agreement with the experimental results, except for Zone 5 over 20° flow direction. Here, the CFD results provided significantly larger y-directional force components. The difference is caused by the extreme wind suction in the vicinity of the last internal edge, where the WT measurements did not detect peak suction forces in contrast to the CFD results.
- The difference of the numerical and experimental $\overline{c}_p$ distributions along the whole surface showed small errors generally, with the exception leeward side of

the internal arches. Only the previously mentioned areas of Zone 5 provided qualitative differences in the distributions. Here, the CFD provided larger wind loads, most probably due to the layout of the measurement points applied in the WT tests. The peak suction induced by the separation from the other internal arches was correctly captured by the CFD quantitatively. Still, the extension of the peak zones was considerably underestimated in some cases. The largest differences in the extension occurred between 30°–50° wind directions. The CFD-based membrane forces also underestimated the WT-based distribution in this regime by approximately 15%.

- The magnitude of the CFD-WT differences strongly correlates with the fluctuating pressure coefficients c_p', reflecting the poorer performance of the applied RANS framework in the case of strong transient structures in the flow field, where scale-resolving methods are known to produce more reliable results. However, at least for preliminary design, GEKO can still provide valuable information.
- Comparing the maximum membrane forces according to the WT and CFD-based wind pressure distributions, it is found that the maximum differences in warp and fill direction are less than 5% and 14%, respectively, representing a pretty good agreement of the pressure distributions from a structural design perspective. The calculated 14% maximal difference is only detected in the fill direction of Zone 2. In the other zones, the differences are considerably smaller.
- Comparing the differences of the CFD- and WT-based distributions with the uncertainties hidden in the resistance side (material properties, material strengths, etc.) and the unconventionally large safety factors applied in tensile membrane design, the CFD simulation of the wind loading of the investigated geometry provides a strong and applicable tool.

Acknowledgments

This work was supported by NKFI (National Research, Development and Innovation Fund) under Grant K138615. The wind tunnel laboratory was supported by the European Union and the Hungarian Government in the framework of Competitive Central-Hungary OP (VEKOP-2.3.3-15-2017-00017 "Establishment of an Atmospheric Flow Laboratory"). The research reported in this paper and carried out at the Budapest University of Technology and Economics has been supported by the Ministry for Culture and Innovation from source of the National Research, Development and Innovation Fund, grant number EKÖP-24-3-BME-223 (University Research Grant Program).

References

[1] Rizzo, F., D'Asdia, P., Lazzari, M., Procino, L. "Wind action evaluation on tension roofs of hyperbolic paraboloid shape", Engineering Structures, 33(2), pp. 445–461, 2011. https://doi.org/10.1016/j.engstruct.2010.11.001

[2] Rizzo, F. "Wind tunnel tests on hyperbolic paraboloid roofs with elliptical plane shapes", Engineering Structures, 45, pp. 536–558, 2012. https://doi.org/10.1016/j.engstruct.2012.06.049

[3] Rizzo, F., D'Asdia, P., Ricciardelli, F., Bartoli, G. "Characterisation of pressure coefficients on hyperbolic paraboloid roofs", Journal of Wind Engineering and Industrial Aerodynamics, 102, pp. 61–71, 2012. https://doi.org/10.1016/j.jweia.2012.01.003

[4] Rizzo, F., Ricciardelli, F. "Design pressure coefficients for circular and elliptical plan structures with hyperbolic paraboloid roof", Engineering Structures, 139, pp. 153–169, 2017. https://doi.org/10.1016/j.engstruct.2017.02.035

[5] Kandel, A., Sun, X., Wu, Y. "Wind tunnel experiment on rectangular-shaped arch-supported membrane structures", Structures, 41, pp. 1515–1531, 2022. https://doi.org/10.1016/j.istruc.2022.05.086

[6] Sun, X., Arjun, K., Wu, Y. "Investigation on wind tunnel experiment of oval-shaped arch-supported membrane structures", Journal of Wind Engineering and Industrial Aerodynamics, 206, 104371, 2020. https://doi.org/10.1016/j.jweia.2020.104371

[7] Pagnini, L., Torre, S., Freda, A., Piccardo, G. "Wind pressure measurements on a vaulted canopy roof", Journal of Wind Engineering and Industrial Aerodynamics, 223, 104934, 2022. https://doi.org/10.1016/j.jweia.2022.104934

[8] De, B., Kumar, A., Mishra, S. K. "Large eddy simulation of wind loading on an anticlastic conical tenisle membrane", Journal of Wind Engineering and Industrial Aerodynamics, 246, 105658, 2024. https://doi.org/10.1016/j.jweia.2024.105658

[9] Papp, B., Kristóf, G., Gromke, C. "Application and assessment of a GPU-based LES method for predicting dynamic wind loads on buildings", Journal of Wind Engineering and Industrial Aerodynamics, 217, 104739, 2021. https://doi.org/10.1016/j.jweia.2021.104739

[10] Pool-Blanco, S. J., Gamboa-Marrufo, M., Hincz, K., Domínguez-Sandoval, C. J. "Wind tunnel tests of an inflated membrane structure. Two study cases: with and without end-walls", Ingeniería Investigación y Tecnología, 23(2), 10, 2022. https://doi.org/10.22201/fi.25940732e.2022.23.2.011

[11] Pool-Blanco, S. J., Hincz, K. "Computational wind analysis of an open air-inflated membrane structure", Pollack Periodica, 18(3), pp. 33–38, 2023. https://doi.org/10.1556/606.2023.00804

[12] Pool Blanco, S. J., Hincz, K. "Computational Wind Engineering of a Mast-supported Tenisle Structure", Periodica Polytechnica Civil Engineering, 66(1), pp. 210–219, 2022. https://doi.org/10.3311/PPci.18656

[13] Hoxey, R. P., Richardson, G. M. "Measurements of wind loads on full-scale film plastic clad greenhouses", Journal of Wind Engineering and Industrial Aerodynamics, 16(1), pp. 57–83, 1984. https://doi.org/10.1016/0167-6105(84)90049-7

[14] Gromke, C., Lippert, O., Eiff, O., Wagner, R. "Analysis of Reynolds Number and Surface Roughness Sensitivity of Surface Pressure on curved Roofs of Biogas Storage Tanks in reduced-scale Wind Tunnel Tests", In: Fachtagung "Experimentelle Strömungsmechanik", München, Germany, 2023, pp. 40-1–40-8. ISBN 978-3-9816764-9-5 [online] Available at: https://gala-ev.org/images/Beitraege/Beitraege2023/pdf/40.pdf [Accessed: 13 August 2025]

[15] Qiu, Y., Sun, Y., Wu, Y., San, B., Tamura, Y. "Surface Roughness and Reynolds Number Effects on the Aerodynamic Forces and Pressures Acting on a Semicylindrical Roof in Smooth Flow", Journal of Structural Engineering, 144(9), 04018140, 2018. https://doi.org/10.1061/(ASCE)ST.1943-541X.0002129

[16] Colliers, J., Degroote, J., Mollaert, M., De Laet, L. "Mean pressure coefficient distributions over hyperbolic paraboloid roof and canopy structures with different shape parameters in a uniform flow with very small turbulence", Engineering Structures, 205, 110043, 2020. https://doi.org/10.1016/j.engstruct.2019.110043

[17] Hincz, K., Pool-Blanco, S. J., Balczó, M. "Wind analysis of a multispan arch-supported tensile membrane structure", Journal of Wind Engineering and Industrial Aerodynamics, 265, 106181, 2025. https://doi.org/10.1016/j.jweia.2025.106181

[18] CEN "EN 1991-1-4:2005 Eurocode 1: Actions on structures - Part 1-4: General actions - Wind actions", European Committee for Standardization (CEN), Brussels, Belgium, 2005.

[19] Menter, F. R. "Two-Equation Eddy-Viscosity Turbulence Models for Engineering Applications", AIAA Journal, 32(8), pp. 1598–1605, 1994. https://doi.org/10.2514/3.12149

[20] Lyu, J., Mason, M. S., Wang, C. M. "Predicting far-lee wind flow characteristics behind a 2D wedge-shaped obstacle: Experiments, numerical simulations and empirical equations", Building and Environment, 194, 107673, 2021. https://doi.org/10.1016/j.buildenv.2021.107673

[21] Younoussi, S., Ettaouil, A. "Calibration method of the k-ω SST turbulence model for wind turbine performance prediction near stall condition", Heliyon, 10(1), e24048, 2024. https://doi.org/10.1016/j.heliyon.2024.e24048

[22] Menter, F. R., Lechner, R., Matyushenko, A. "Best practice: Generalized k-ω two-equation turbulence modeling in Ansys CFD (GEKO)", ANSYS Germany GmbH, Darmstadt, Germany, 2019.

[23] Lukács, E., Vad, J. "Parameter Study of a Loss Reducing Passive Flow Control Method in a Square-to-square Sudden Expansion", Periodica Polytechnica Mechanical Engineering, 67(3), pp. 204–213, 2023. https://doi.org/10.3311/PPme.22389

[24] Hincz, K. "Determination of the Cutting Patterns of Prestressed Tent Structures", Revista Portuguesa de Engenharia de Estruturas, 47, pp. 45–49, 2000. [online] Available at: https://www.researchgate.net/publication/336610165_Determination_of_the_cutting_patterns_of_prestressed_tent_structures [Accessed: 13 August 2025]